



# Evolution of Microstructure and Mechanical Properties of a Stainless-Steel Powder/Wire Mesh Composite Porous Strip for Powder Densification

SHENGCUN LIN<sup>1,2</sup> and ZHAOYAO ZHOU<sup>1,3</sup>

1.—Guangdong Key Laboratory for Processing and Forming of Advanced Metallic Materials, School of Mechanical and Automotive Engineering, South China University of Technology, Guangzhou 510640, China. 2.—School of Automotive Engineering, Liuzhou Vocational & Technical College, Liuzhou 545005, China. 3.—e-mail: zhyzhou@scut.edu.cn

A device that automatically feeds powder and wire mesh was developed to produce a stainless-steel powder/wire mesh composite porous strip (PWMCS). The PWMCS was cut into three same-sized samples, whereby one sample comprised the original strip with no further processing, one sample was rolled for 15 passes, and the last sample was rolled twice for 15 passes and re-sintered; thus, the three samples displayed different porosities. X-ray diffraction, optical microscopy, and scanning electron microscopy were used to investigate the microstructure and phase transformation of the samples. Tensile experiments were also conducted. The results revealed that with the added rolling deformation, more  $\gamma$ -austenite changed to  $\alpha'$ -martensite, and both the yield and ultimate tensile strengths increased markedly ( $361.4 \pm 10.5\%$  and  $189.5 \pm 14.7\%$  increases, respectively). All three samples exhibited ductile fracture, and the dimples varied from large and deep in the initial state to shallow appearance in the final state.

## INTRODUCTION

Powder rolling technology is a process in which metal powder is continuously fed by a feeding device into the gap between two rollers moving in opposite rotation directions but in the same plane.<sup>1–4</sup> Thus, with the aid of pressure, the rollers press the powder into a continuous raw strip of a certain thickness, porosity, and the appropriate mechanical strength, and a porous material is obtained after sintering.<sup>5,6</sup> Powder rolling technology is currently the most common technique used to prepare porous materials. In previous studies,<sup>7–9</sup> porous materials were prepared by mixing one or more types of powder. For example, Gogaev et al.<sup>10</sup> reported a method for producing strips by titanium powder

rolling, while Floriano et al.<sup>11</sup> used  $\text{MgH}_2$  powders containing different additives during cold rolling. Moreover, Sakai et al.<sup>12</sup> reported powder rolling of aerosolized gas-atomized lead–tin and lead–tin–calcium alloy powders as raw materials to produce collector plates for lead-acid batteries.

Rolling porous strips are sintered for sufficient strength and plasticity, which is advantageous for follow-up processing.<sup>13–15</sup> However, although the mechanical properties of a rolling porous strip can be improved after sintering, compared with the theoretical density, the internal structure of a sintered porous strip with lower mechanical properties still possesses porous characteristics.<sup>16–18</sup> Therefore, subsequent densification is indispensable to attain the required mechanical properties.<sup>19–22</sup>

The common methods for the densification of porous materials include repeated cold rolling and sintering, hot rolling, and forging.<sup>23–28</sup> Currently, the densification of porous materials is attracting significant attention, owing to its important effect on both theoretical study and practical

application.<sup>29–31</sup> For example, Deshmukh et al.<sup>32</sup> applied the upper-bound technique coupled with the plasticity theory of porous metals to analyze the cold densification rolling of a sintered porous metal strip. They considered plane-strain deformation and incorporated work-hardening effects during cold rolling. Kwon et al.<sup>33</sup> studied the densification and grain growth of porous alumina compacts during various high-temperature processes and obtained experimental data on the densification and grain growth of alumina powder during hot pressing. Jang et al.<sup>34</sup> studied the microstructure evolution and densification kinetics of Al<sub>2</sub>O<sub>3</sub>-SiC powder composites with two different SiC powders, revealing that the densification process was divided into three stages: the first stage was characterized by the absence of grain growth and changes in the pore size; the second stage displayed both rapid pore coarsening and grain growth; and the third stage displayed pore shrinkage and slow grain growth. Finally, Wang et al.<sup>35</sup> studied the effects of agglomerates on the densification behavior and microstructural evolution of a cube of copper particles in solid-state sintering, revealing that the densification of the sintering system decreases with increasing agglomeration.

In contrast, literature on the preparation of porous strips by composite rolling and sintering of wire mesh and powder and that of the changes in mechanical properties and microstructure in densification is very scarce. With these facts in mind, in this study a device was innovatively developed that could automatically feed powder and wire mesh with an ultrasonic vibrator and a composite porous strip was fabricated by rolling and sintering of stainless-steel powder and wire mesh (PWMCS). Furthermore, multi-pass horizontal rolling and secondary sintering were performed to improve the mechanical properties of the PWMCS. Finally, tensile experiments were performed to study the mechanical and microstructure properties during densification together with the fracture process of the PWMCS.

## EXPERIMENTAL SECTION

### Preparation of the Stainless-Steel Powder and Wire Mesh Composite Porous Strip

The employed 304 stainless-steel wire mesh was plain-woven and comprised a mesh count of 80, wire diameter of 95  $\mu\text{m}$ , mesh size of 220  $\mu\text{m}$ , and thickness of 0.18 mm (Fig. 1a). The irregular water-atomized 304 stainless-steel powder comprised a mesh count of 200 (Fig. 1b).

As illustrated in Fig. 1a and c device was designed and developed to feed powder and wire mesh automatically and continuously and installed on a vertical rolling machine to form a rolling system that does not require manual participation. Two wires were connected to an ultrasonic vibrator at one end and an ultrasonic generator (working

frequency range, 0–100 Hz) at the other. The moving plate moved along the inclined plate and reached the bottom of the straight plate, so that the distance between the bottoms of the straight and moving plates was zero. Thus, the metal powder did not leak out when the ultrasonic vibrator was vibrating.

Figure 1d illustrates the rolling principle of the porous strip. The wire mesh runs along the straight plate of the powder box and passes through the gap between the two rollers; the wire mesh is clamped when there is no gap between the two rollers. The distance ' $d$ ' between the bottoms of the straight and moving plates is adjusted in advance, and the powder box is filled with metal powder. The rolling machine and ultrasonic generator start synchronously, and the wire mesh is squeezed and moved down immediately, owing to the reverse rotation of the two rollers. At this time, the vibration of the ultrasonic vibrator head causes the powder box to vibrate, so that the metal powder falls onto the rollers through distance  $d$ . This metal powder is rolled synchronously with a metal wire mesh to afford a porous strip. Finally, the PWMCS is prepared after the porous strip is sintered at a high temperature of 1330°C, held for 2 h and naturally cooled to room temperature in a vacuum furnace.

## DENSIFICATION PROCESS

The densification process of the PWMCS is depicted in Fig. 2. First, the distance  $d$  was adjusted to 0.15 mm, the ultrasonic generator frequency was set to 60 Hz, and the porous strip was prepared by rolling. The porous strip was then sintered at 1330°C in a WHS-20 vacuum furnace in which the heat was preserved for 2 h. A PWMCS with a thickness of 0.8 mm was thus prepared, and three samples with dimensions 130 mm  $\times$  85 mm were cut from it and processed as follows: Sample 1, did not undergo any subsequent processing and retained the characteristic dimensions of the original porous strip; Sample 2, with 37.5% reduction in thickness and final area dimensions of 180 mm  $\times$  90 mm, was horizontally rolled at room temperature for 15 passes; and Sample 3, with final dimensions of 0.38mm (thickness)  $\times$  210 mm  $\times$  93 mm, was first horizontally rolled at room temperature for 15 passes (as in Sample 2), sintered at 1330°C with heat preservation for 2 h, and finally horizontally rolled at room temperature for another 15 passes. The maximum rolling force of the horizontal rolling machine was 240 tons and the roll gap of each pass was 90% of the thickness of the specimen to be rolled at every rolling stage. Notably, the length of the rolling direction increased, while the thickness decreased during the entire process.

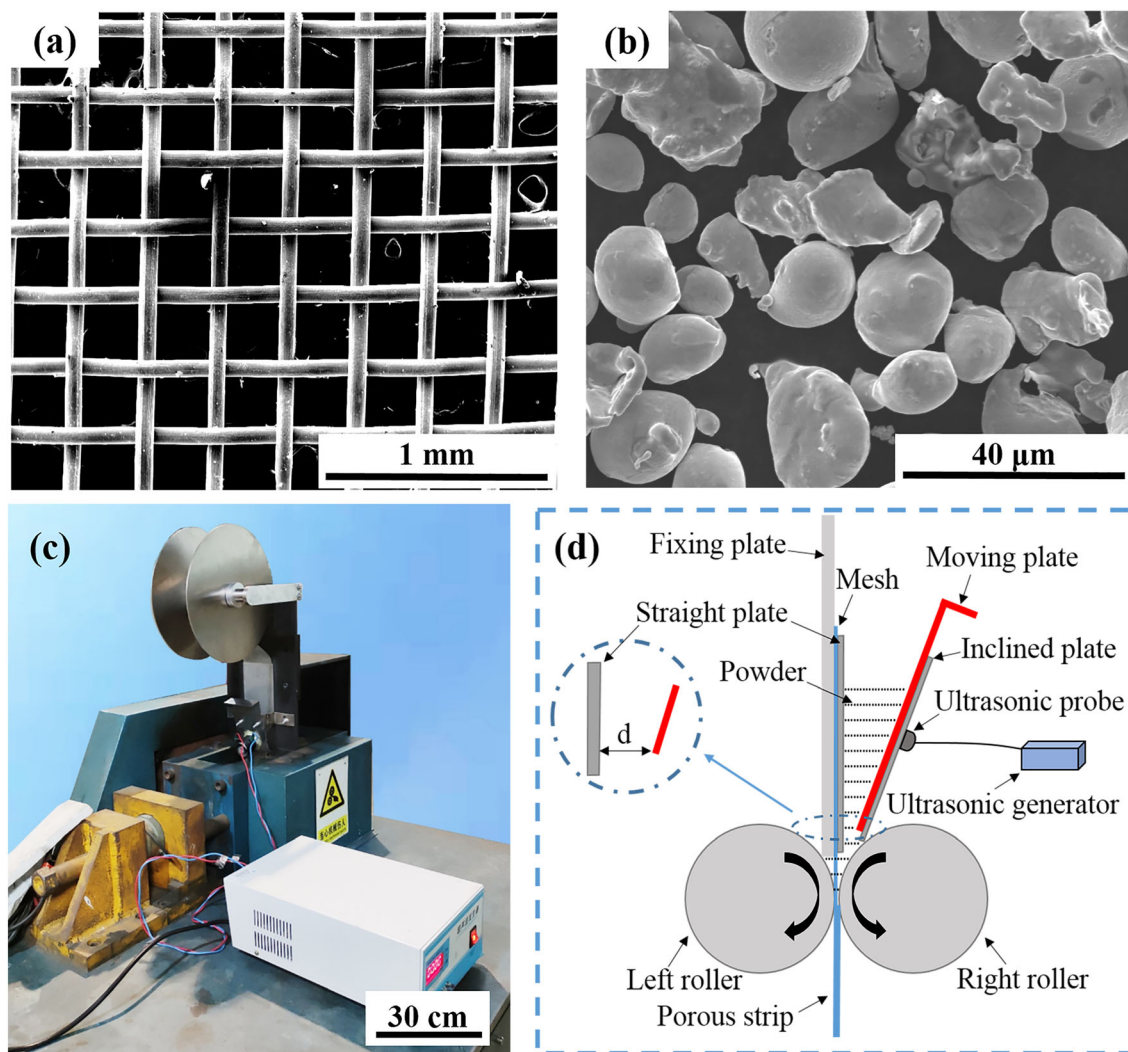


Fig. 1. Scanning micrographs of the (a) 304 stainless-steel wire mesh and (b) 304 stainless-steel powder. (c) Equipment setup used to prepare the porous strip, and (d) rolling principle of the porous strip.

### CHARACTERIZATION TESTS

The phase compositions were identified using an x-ray diffractometer (D8 Advance, Bruker AXS, Germany) with a Cu-K $\alpha$  radiation source at 50 kV and 150 mA. The scan rate was 12° min<sup>-1</sup> over the range from 20° to 100° with a depth of 2–3  $\mu$ m and it was positioned in the center location with a step width of 0.013°. Three small samples with dimensions 8 mm  $\times$  8 mm were cut from each sample for the XRD test, and 304 stainless-steel powder and 304 stainless-steel wire mesh were also examined. To identify the microstructures, 300–2000 mesh SiC emery paper and a diamond suspension with a particle size of 0.25  $\mu$ m were used to mechanically grind and polish the surfaces of the samples, after which etching was performed using aqueous solutions of ferric chloride. The microstructures were observed by optical microscopy (Leica DMI 5000, Leica, Wetzlar, Germany), while the fracture morphologies of the samples subject to tensile testing

were observed by scanning electron microscopy (SEM, Quanta200, FEI, Eindhoven, Holland). Ten tensile samples were wire cut from each type of sample. The tensile tests were conducted at room temperature (approximately 25°C) on an electronic universal mechanical testing machine (UTM5105, SUNS, Guangdong, China) at a constant crosshead speed of 1 mm min<sup>-1</sup>. Vickers hardness measurements were carried out on a micro-hardness instrument (DHV-1000Z, SCTMC, Shanghai, China) at a load of 10 kg and a dwelling time of 15 s. Ten small samples with dimensions 10 mm  $\times$  10 mm were cut from each type of sample for hardness tests. Five points on the surface of each small sample were selected for testing, and the average Vickers hardness of the fifty points was taken as the result. The most common method for calculating porosity is the mass volume method. The preconditions of using the mass volume method to measure sample porosity are regular shape and single base material composition. In this work, ten small samples with



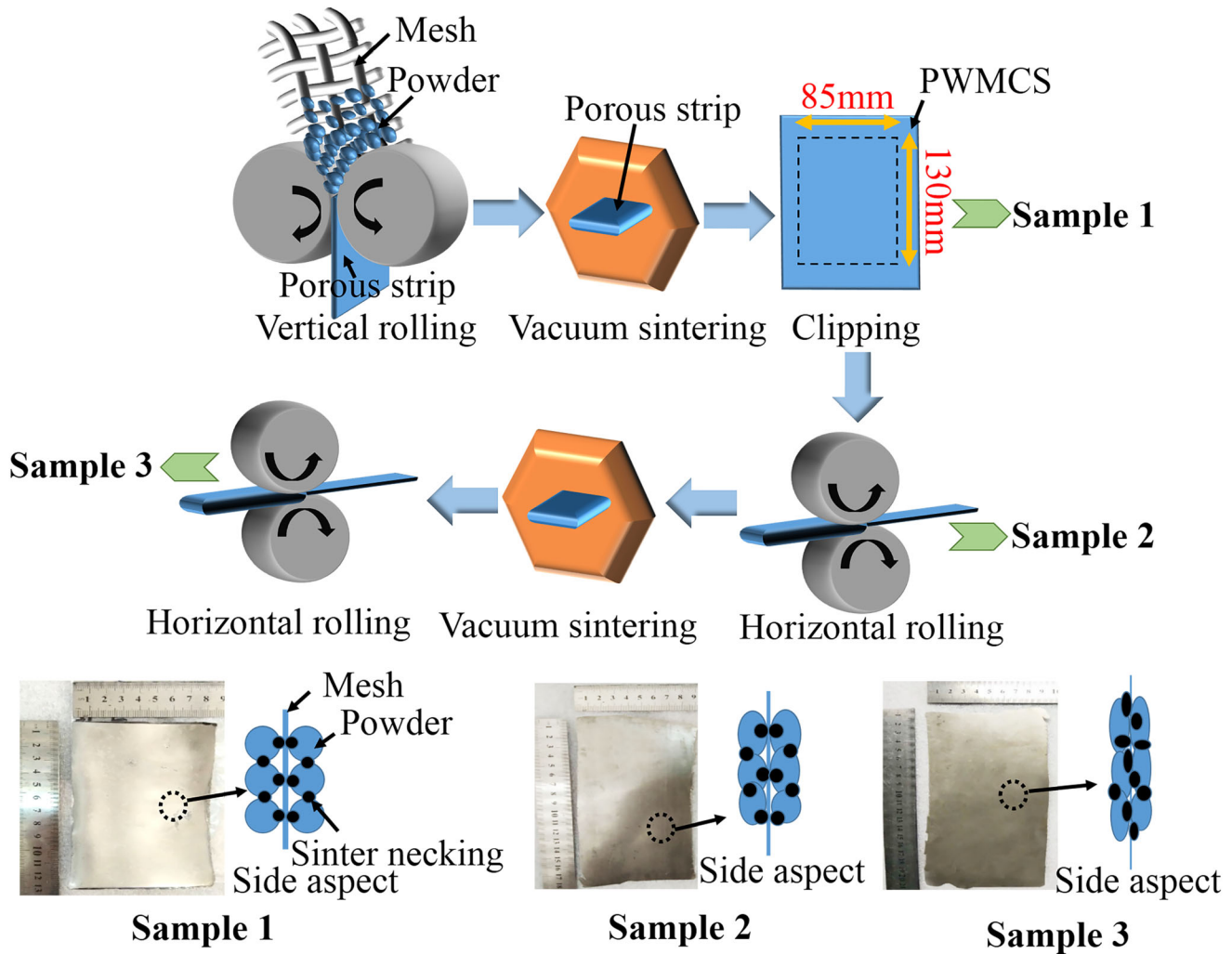


Fig. 2. Powder/wire mesh composite porous strip densification process.

dimensions of  $h$  (thickness)  $\times 10 \text{ mm} \times 10 \text{ mm}$  were cut from each of the three samples mentioned above as the test samples. It can be seen that the raw material of these small samples with regular shapes is 304 stainless steel, so the mass volume method was used to measure the porosity using the equation

$$P(\%) = \left(1 - \frac{M}{\rho v}\right) \times 100, \quad (1)$$

where  $P$  is the average porosity of the sample,  $M$  is the mass of the sample (g),  $v$  is the volume of the sample ( $\text{cm}^3$ ), and  $\rho$  is the density of 304 stainless steel ( $\text{g cm}^{-3}$ ).

## RESULTS AND DISCUSSION

### X-ray Diffraction Profiles

XRD curves of 304 stainless-steel powder and 304 stainless-steel wire mesh are shown in Fig. 3.

Because the powder and wire mesh were 304 stainless steel, which is a type of austenitic stainless steel in which austenite exists at room temperature, it can be judged that the peaks of the powder and wire mesh XRD were austenite. This judgment can be further verified by comparison with the standard austenite and martensite pdf cards in Fig. 3. Numerous studies<sup>36–39</sup> have reported that austenite changes to martensite due to plastic deformation, and thus, XRD analysis was performed to investigate the evolution of phases in the three samples. In the XRD curves of Sample 1 (black spectrum), marked peaks of  $\gamma$ -austenite were observed with the  $\gamma$  (111) peak being the most significant and weak  $\alpha'$ (110). This indicated that Sample 1 was mainly composed of austenite and a little martensite. Sample 1 was prepared by vertical composite rolling of 304 austenite stainless-steel powder and 304 austenite stainless-steel wire mesh, sintered at a high temperature of  $1330^\circ\text{C}$  and held for 2 h, then

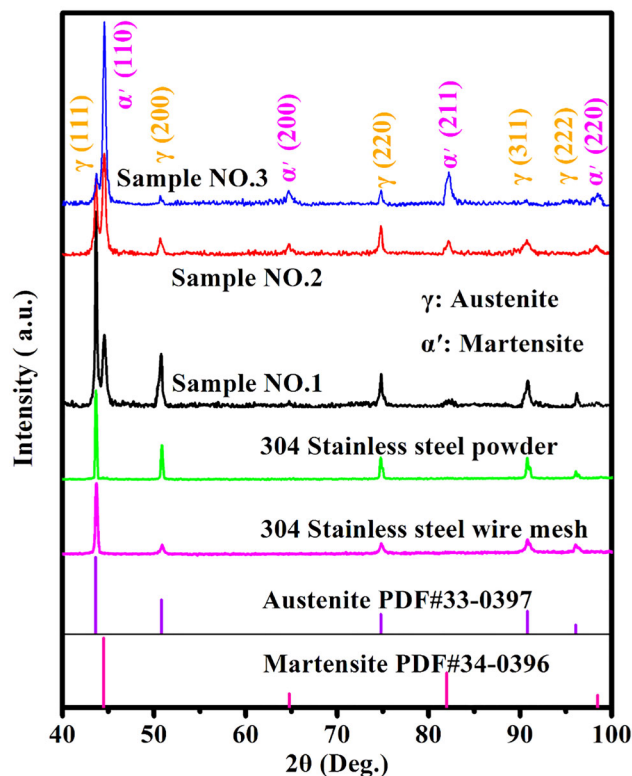


Fig. 3. XRD patterns of the three samples, 304 stainless-steel powder, wire mesh, and  $\gamma$ -austenite and  $\alpha'$ -martensite pdf cards.

naturally cooled to room temperature in a vacuum furnace. The chemical composition of Sample 1 in weight percent (wt.%) was Fe-19.03Cr-0.02C-0.25Si-9.38Ni-0.87Mn-0.02P-0.02S. It is well known that austenite is in a stable state at sintering temperature. The addition of Cr, Ni, Mn, and other elements, on the one hand, could enhance the stability of austenite by solid solution in austenite, so that the austenite phase could be retained to room temperature;<sup>39-43</sup> on the other hand, these elements moved the isothermal transition curve of austenitic steel to the right,<sup>39,40,44,45</sup> and the austenite zone was enlarged.<sup>46,47</sup> Therefore, austenite did not pass through the ferrite phase transformation zone and convert to ferrite, even with slow cooling. At the same time, the temperature of the martensitic transformation point was calculated to be about 106°C by using the  $M_s$  formula,<sup>48</sup> and the  $M_s$  temperature was lowered significantly.<sup>44,49,50</sup> Therefore, most of the austenite was retained during furnace cooling. However, due to the inhomogeneity of the sample composition, there was a small amount of component segregation in local areas. This part of the austenite was in an unstable thermodynamic state, and is known as supercooled austenite.<sup>46,51,52</sup> When the sample cooled to the martensite transformation temperature, the

supercooled austenite transformed into martensite through solid phase transformation,<sup>46,51,53</sup> so the martensite peak was also observed in the XRD curve of Sample 1. After 15 rolling passes (Sample 2), the  $\gamma$ -austenite peaks were weakened, and peaks characteristic of  $\alpha'$ -martensite were observed (red spectrum). Notably, both  $\alpha'$ -martensite and  $\gamma$ -austenite were present in Sample 2, further proving that the fundamental reason for the transformation of  $\gamma$ -austenite into  $\alpha'$ -martensite is the plastic deformation<sup>39,45</sup> caused by rolling. In Sample 3, the  $\gamma$  (111) peak visibly decreased and the other  $\gamma$ -austenite peaks almost disappeared (blue spectrum). In contrast, the strength of the  $\alpha'$ -martensite peaks increased markedly. According to ASTM Standard E562-02, manual point counting<sup>53,54</sup> was adopted to measure the volume fraction of austenite and martensite in the three samples, and five fields per sample were analyzed at 200  $\times$  magnification. The volume fraction of austenite in Sample 1 was 91.2%  $\pm$  0.5%, and that of martensite in Samples 2 and 3 were 58.7%  $\pm$  0.3% and 93.0%  $\pm$  0.8%, respectively. These observations implied that a large amount of  $\gamma$ -austenite was converted to  $\alpha'$ -martensite with the increase in rolling deformation.

## MICROSTRUCTURAL PROPERTIES

The optical microstructures of the three samples (Fig. 4) reveal that with continuous rolling, most of the numerous pores that were present in Sample 1 faded away in Sample 3, owing to the mechanical bonding formed during rolling. Moreover, Sample 1 mainly consisted of austenite phase; however, after multi-pass rolling, a growing content of the austenite phase was transformed into the martensite phase so that Sample 3 comprised both austenite and martensite phases. Thus, as seen in the magnified image in Fig. 4b, Sample 1 comprised the austenite phase with an apparent grain boundary, a few twins that were unevenly distributed, and many large holes. Little martensite phases also can be found. On the other hand, Sample 2 underwent plastic deformation after 15 rolling passes and some complete austenite grains still emerged; however, the other grains were transformed into acicular martensite (Fig. 4d). Moreover, owing to the cold rolling process,<sup>45</sup> the holes in this sample shrank and were significantly smaller than those of Sample 1. Finally, the martensite phase predominated in Sample 3 (Fig. 4f), as most of the austenite was transformed into martensite, owing to the effect of rolling strengthening after an additional set of 15 rolling passes. These microstructures accurately corroborate the XRD results displayed in Fig. 3.



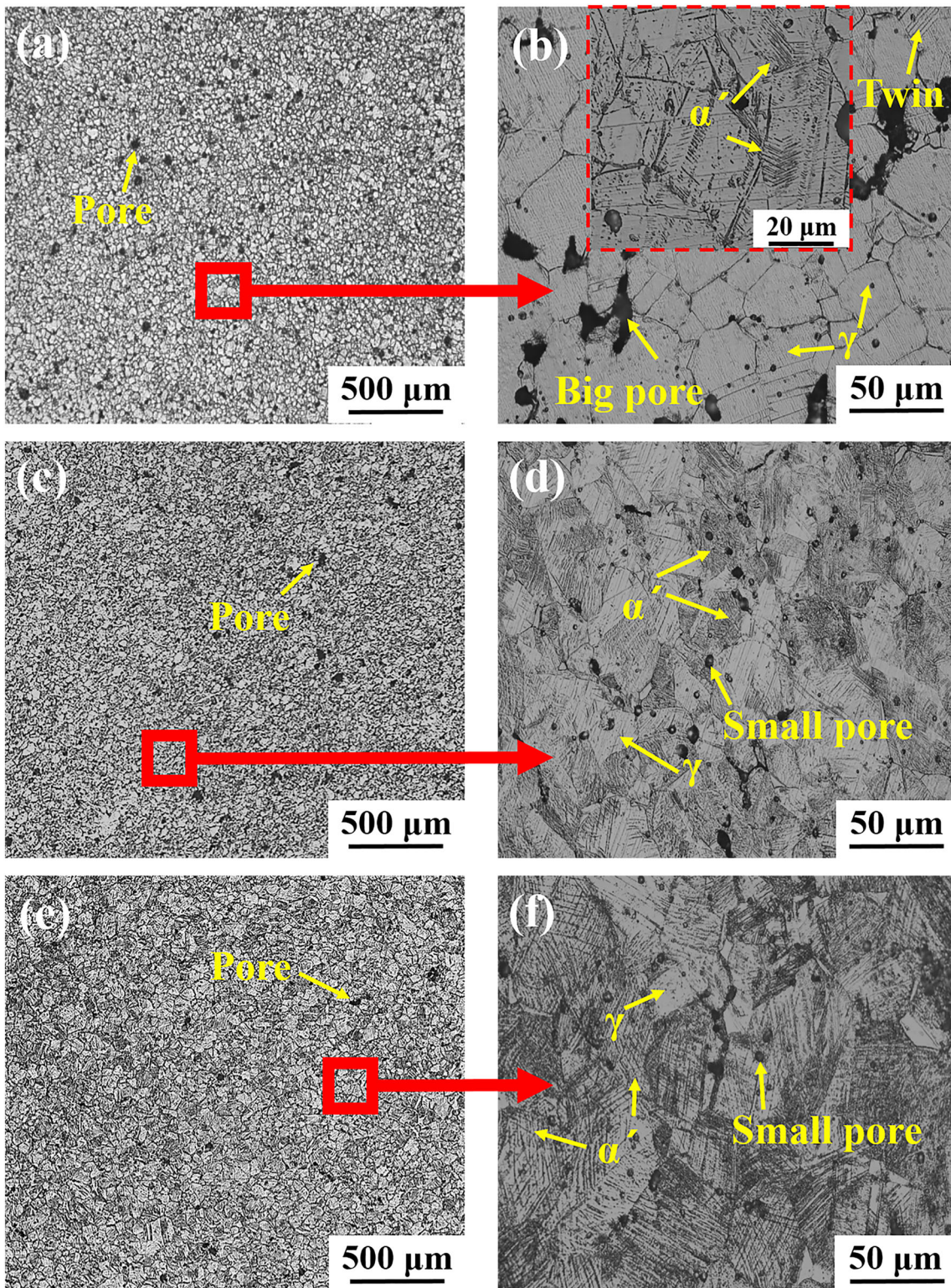


Fig. 4. Optical microstructures of (a, c, e) Samples 1, 2, and 3, respectively and (b, d, f), their respective magnified red-square areas.

Figure 5 shows the scanning electron micrographs of the three samples. The austenite phase with visible grain boundaries is observed in Sample 1 together with a host of large deep pores (Fig. 5a).

On the other hand, martensite phases are observed in Sample 2 (Fig. 5b), indicating that plastic deformation induced martensitic transformation<sup>38,39</sup> after 15 rolling passes. Moreover, the large deep



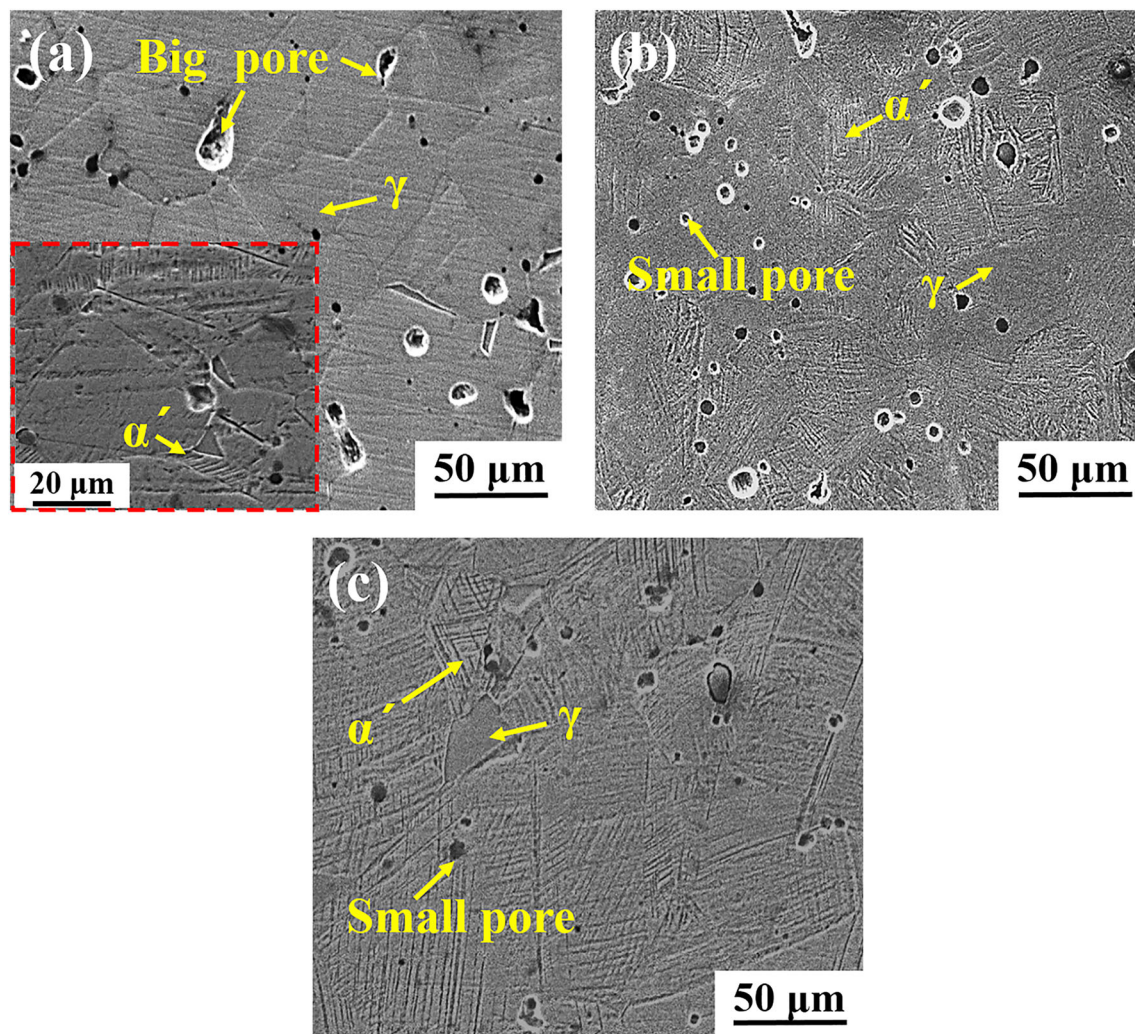


Fig. 5. Scanning electron micrographs of (a) Sample 1, (b) Sample 2, and (c) Sample 3.

pores observed in Sample 1 disappeared and only some small pores are distributed on the sample surface. The martensite content formed from austenite is significantly greater in Sample 3 after a second set of 15 rolling passes was employed (Fig. 5c). The evolution rule of the SEM microstructures (Fig. 5) is in good agreement with the corresponding metallographic microstructures (Fig. 4). Thus, it can be concluded that the plastic deformation<sup>38,39</sup> of the sample caused by rolling induced martensitic transformation together with pore shrinkage and disappearance.

### TENSILE PROPERTIES

Figure 6a displays the true stress–strain curves of the samples after tensile testing. All three samples exhibited a marked stress strengthening process during the plastic deformation stage, because the wire mesh acted as the reinforcing material.<sup>55</sup> This was attributed to the sintering necks that were formed between adjacent wire mesh–powder, wire mesh–wire mesh, and powder–powder in the porous

strip after sintering at high temperature (Fig. 6b), making the strip resistant to tension and deformation during the stretching process.<sup>56,57</sup>

The tensile test results are presented in Table I, wherein the yield strength and ultimate tensile strength of Sample 1 were  $151.1 \pm 12.4$  MPa and  $355.6 \pm 16.3$  MPa, respectively. Compared with the values for Sample 1, the yield strength and ultimate tensile strength of Sample 2 increased significantly after one set of 15 rolling passes, while the plasticity was reduced. In fact, compared with Sample 1, Sample 2 displayed a  $331.8 \pm 10.3\%$  improvement in yield strength ( $151.1 \pm 12.4$  MPa versus  $652.5 \pm 11.8$  MPa, respectively) and  $114.9 \pm 11.6\%$  improvement in the ultimate tensile strength ( $355.6 \pm 16.3$  MPa versus  $764.5 \pm 15.4$  MPa, respectively), while its total elongation of fracture was  $13.3 \pm 1.8\%$ , which is  $45.5 \pm 1.6\%$  less than that of Sample 1. The principal reason for work hardening is the deformation-induced martensitic transformation.<sup>58,59</sup> It can be observed that the thickness decreased by 37.5% after 15 rolling passes and, owing to this

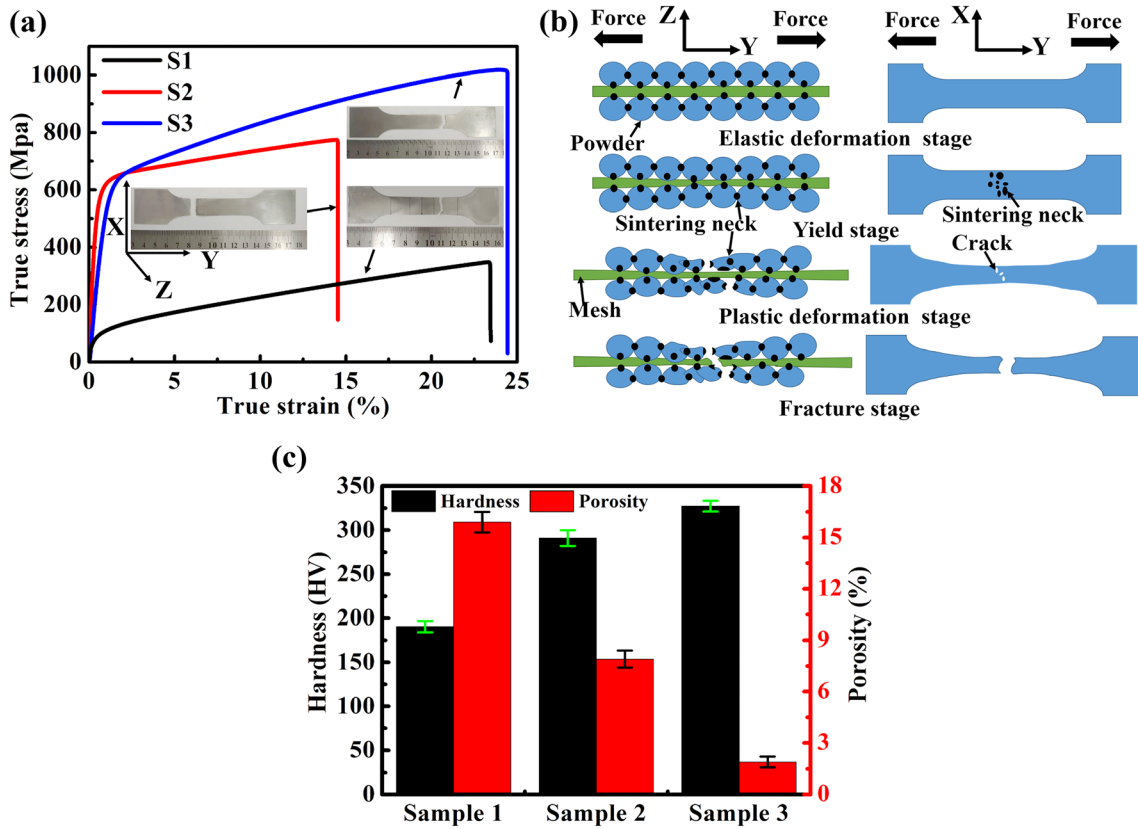


Fig. 6. (a) True stress-strain curves of the three samples, (b) fracture principle of the sample during the tensile process, and (c) porosity and Vickers hardness of the three samples.

Table I. Characteristics of the mechanical properties of the three samples

Sample number	Sample thickness (mm)	Strength (MPa)		Plasticity (%)		Vickers hardness (HV)	Porosity (%)
		Yield strength	Ultimate tensile strength	Section shrinkage rate	Total fracture elongation		
S1	0.80	151.1±12.4	355.6±16.3	23.9±1.3	24.4±1.4	190.4±6.2	15.9±0.6
S2	0.50	652.5±11.8	764.5±15.4	9.6±1.4	13.3±1.8	290.9±8.9	7.9±0.5
S3	0.38	697.2±11.6	1029.4±13.0	23.1±1.1	25.3±1.2	327.3±6.0	1.9±0.3

deformation-induced martensitic transformation, work hardening occurred that resulted in better strength; the additional mechanical bonding caused by rolling was also key to this improved strength.<sup>60,61</sup> Various studies have reported that the generation of martensite phases in materials after rolling weakens the plasticity.<sup>62–64</sup> The metallographic microstructure, SEM microstructure, and XRD pattern results revealed that  $\gamma$ -austenite changed into  $\alpha'$ -martensite during rolling. Therefore, it can be supposed that owing to the increased  $\alpha'$ -martensite content, the plasticity of Sample 2 decreased.<sup>36,65</sup>

Compared with that of Sample 2, the plasticity of Sample 3 improved noticeably, so that the total fracture elongation increased to  $25.3 \pm 1.2\%$ , the yield strength was  $697.2 \pm 11.6$  MPa, and the ultimate tensile strength was  $1029.4 \pm 13.0$  MPa. Moreover, the second stage of high-temperature sintering played a crucial role in enhancing the mechanical properties. Thus, the atoms in Sample 3 moved violently under the action of high-temperature sintering, and promoted the generation of more and larger powder-wire mesh and powder-powder sintering necks. Because the second high-temperature sintering reinforced the metallurgical bonding and afforded stronger powder-powder and powder-wire mesh combinations, Sample 3 was able to



withstand greater plastic deformation and tensile strength before breaking. Thus, its total fracture elongation increased, and its strength was the greatest of all three samples. Moreover, after the second set of 15 rolling passes, work hardening also occurred, and the increased mechanical bonding resulted in higher densification of the internal structure, which is also vital for increasing the strength.<sup>66,67</sup>

Figure 6b reveals that all three samples experienced four stages in the tensile test, namely elastic deformation, yield, plastic deformation, and fracture stages. Necking also occurred, with measured section shrinkage rates of  $23.9 \pm 1.3\%$ ,  $9.6 \pm 1.4\%$ , and  $23.1 \pm 1.1\%$  for Samples 1–3, respectively.<sup>68</sup> These results implied that all the fractures in all three samples were ductile fractures.<sup>69–72</sup> In the yield stage, the sample resisted the continuous tensile force to produce elastic deformation. During the plastic deformation stage, deformation hardening enhanced the ability of the sample to resist further deformation and led to a distinct increase in the stress.<sup>73</sup> Thus, with the continual local yielding and redistribution of the tensile stress, the fracture of the sample started from the holes in the weak area and then propagated into the surrounding area until the sample broke immediately.

The Vickers hardness and porosity values of the three samples are shown in Fig. 6c. Because of rolling, the pores of the sample shrank and closed gradually, leading to a decline in porosity. Work hardening increases the hardness of metals.<sup>74–77</sup> Moreover, plastic deformation<sup>38,39</sup> occurs during rolling, so that  $\gamma$ -austenite gradually changes to  $\alpha'$ -martensite.<sup>78,79</sup> Thus, it is concluded that martensitic transformation is the main reason for work hardening, wherein the increased hardness helps enhance the Vickers hardness of the samples.<sup>80,81</sup>

## FRACTURE MORPHOLOGY ANALYSIS

Figure 7 illustrates the fracture morphologies of the samples after tensile testing. Sample 1 presented numerous large deep holes surrounded by dimples (Fig. 7a), consistent with its porous nature. In light of the fracture mechanism of porous material, the pores surrounded by dimples are the first position of fracture.<sup>82</sup> Thus, following the first set of 15 rolling passes, the large deep pores disappeared in Sample 2. Indeed, in this sample some small pores surrounded by numerous small dimples were observed, and the fracture morphology demonstrated the basic characteristics of ductile fracture (Fig. 7c).<sup>68</sup> Finally, most of the pores closed after the second high-temperature sintering and second set of 15 rolling passes (Sample 3), and the tensile fracture displayed a dimple pattern characteristic of ductile fracture (Fig. 7e).<sup>83</sup>

The images of the magnified areas revealed that the dimples in Sample 1 were large and deep (Fig. 7b). Sintering necks between the wire mesh

and powder were formed after high-temperature sintering, and wire mesh necking occurred in the dimples after the tensile test was performed. This is in accordance with the order of fracture (i.e., the crack started from the holes and extended to the positions where the mesh and powder were sintered together), confirming that necking occurred during the tensile test and wire mesh necking existed in the dimple. When the sample was subjected to 15 rolling passes (Sample 2), the large deep pores shrank and even faded away (Fig. 7d). Here the rolling force resulted in closer mechanical bonding between the wire mesh and powder and the powder and generated powder; therefore, no wire mesh necking was observed in Sample 2 after fracture. Moreover, the number of large deep dimples was significantly reduced and the size of the dimples was markedly diminished. Thus, in this sample, shallow dimples were clearly visible, while a few deep dimples were still observed. Compared with those of Sample 2, the dimples on the fracture of Sample 3 were shallower (Fig. 7f). This can be linked to the further metallurgical and mechanical bonding between the wire mesh and powder and the powder and powder formed by the joint action of the second high-temperature sintering and second set of 15 rolling passes. Thus, more sintering necks participated in the tension resistance and shallow dimples were finally generated so that of the three samples,<sup>84–86</sup> Sample 3 exhibited the highest tensile strength and plasticity after fracture.

From the microscopic viewpoint of the fractured samples, the fractures of all the samples comprised ductile dimples. Thus, it can be considered that all the fractures of the three samples were ductile fractures, which is consistent with the section shrinkage rate results.<sup>75</sup> In general, the tensile fracture morphologies of the samples changed from large holes surrounded by large and deep dimples at the initial state of the test to narrowed holes and numerous shallow dimples at the end of the test.

## CONCLUSION

A novel stainless-steel powder/wire mesh composite porous strip (PWMCS) was prepared by using a self-developed device that can automatically feed powder and wire mesh without manual intervention. The microstructure and mechanical properties of this PWMCS during densification were studied. Based on the above results and discussion, the following conclusions can be drawn:

1. The samples underwent deformation and martensite phase transformations during rolling, and the amount of martensite increased with increasing rolling deformation. In addition, the large deep holes observed in the original (unprocessed) sample disappeared in the final (most processed) sample, leading to porosity reduction.
2. Owing to rolling deformation, the  $\gamma$ -austenite

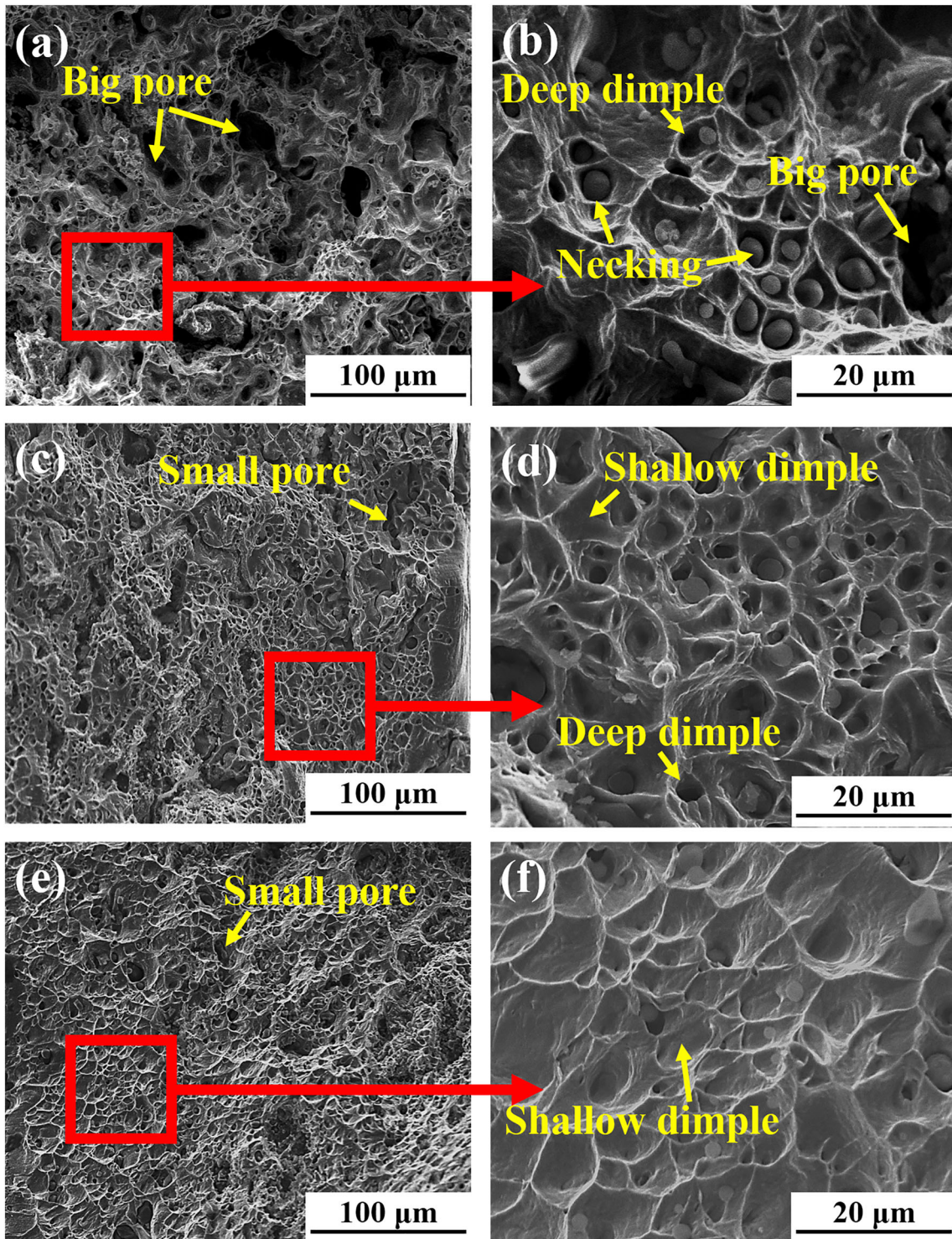


Fig. 7. Fracture morphologies of (a, c, e) Samples 1, 2, and 3, respectively, and (b, d, f) their respective magnified *red-square* areas.

changed to  $\alpha'$ -martensite, which led to pronounced strength enhancement of the processed samples. Indeed, the increased mechanical bonding brought about by the rolling force is a non-negligible factor for the marked increase in the material strength.

3. Because the added  $\alpha'$ -martensite led to poor

plasticity, the elongation at the total fracture of Sample 2 was lower than that of Sample 1. Under the combined secondary sintering and second set of 15 rolling passes, the internal structure of the sample exhibited further cohesiveness. Simultaneously, metallurgical bonding was improved and the total fracture elongation



of Sample 3 increased significantly. Indeed, the hardness of this sample increased by  $71.9 \pm 7.5\%$ , which was attributed to work hardening caused by rolling.

4. All three samples experienced elastic deformation, yield, plastic deformation, and fracture stages. The cracks began in the weak areas comprising pores, expanded to the periphery, and broke immediately. The emergence of fractures with dimples, classified as ductile fracture, was observed, wherein the dimples changed from deep and large in Sample 1 (initial state) to shallow in Sample 3 (final state).

### ACKNOWLEDGEMENT

The authors acknowledge financial support from the Science and Technology Program of Guangzhou, China (No. 201604016015).

### CONFLICT OF INTEREST

The authors declare that they have no conflict of interest.

### REFERENCES

1. R.T. Dec, A. Zavaliangos, and J.C. Cunningham, *Powder Technol.* 130, 265. (2003).
2. X. Luo, and Y. Liu, *JOM* 68, 3078. (2016).
3. Y. Zhao, D. Chen, D.K. Li, J.G. Peng, and B. Yan, *Metals* 8, 91. (2018).
4. A. Mazor, L. Orefice, A. Michrafy, A. de Ryck, and J.G. Khinast, *Powder Technol.* 337, 3. (2018).
5. G.M. Derkacheva, G.Y. Kalutskii, and R.V. Minakova, *Powder Metall. Met. Ceram.* 39, 202. (2000).
6. G.A. Vinogradov, *Powder Metall. Met. Ceram.* 41, 517. (2002).
7. I. Oh, N. Naoyuki, N. Nomura, N. Masahashi, and S. Hanada, *Scr. Mater.* 49, 1197. (2003).
8. S. Chikosha, T.C. Shabalala, and H.K. Chikwanda, *Powder Technol.* 264, 310. (2014).
9. H. Xu, N. Zou, and Q. Li, *JOM* 69, 1236. (2017).
10. K.A. Gogaev, V.A. Nazarenko, V.A. Voropaev, Y.N. Podrezov, D.G. Verbilo, O.S. Koryak, and I.Y. Okun, *Powder Metall. Met. Ceram.* 48, 652. (2009).
11. R. Floriano, D.R. Leiva, S. Deledda, B.C. Hauback, and W. Botta, *Int. J. Hydrogen Energy* 38, 16193. (2013).
12. M. Sakai, Y. Kondo, S. Minoura, T. Sakamoto, and T. Hirasawa, *J. Power Sources* 185, 559. (2008).
13. M. Abdullah, L. Jamaludin, K. Hussin, M. Bnhussain, and M.I. Ahmad, *Int. J. Mol. Sci.* 13, 4388. (2012).
14. S.V. Smirnov, A.V. Nesterenko, V.N. Bykov, and V.G. Mikhailov, *Russ. Metall.* 2007, 506. (2007).
15. B. Zhou, W. Yuan, J.Y. Hu, Y. Tang, L.S. Lu, and B.H. Yu, *Trans. Nonferrous Met. Soc. China* 25, 2003. (2015).
16. J. Sun, Y. Yang, and W. Di, *Mater. Des.* 49, 545. (2013).
17. D.A. Ivanov, S.D. Shlyapin, G.E. Val'Yano, and L.V. Fedorova, *Refract. Ind. Ceram.* 58, 538. (2018).
18. A.P. Rubshtein, I.S. Trakhtenberg, E.B. Makarova, E.B. Triphonova, D.G. Bliznets, L.I. Yakovenkova, and A.B. Vladimirov, *Mater. Sci. Eng. C* 35, 363. (2014).
19. K. Ren, Q.K. Wang, Y.L. Lian, and Y.G. Wang, *J. Alloys Compd.* 747, 1073. (2018).
20. S.H. Deng, R.D. Li, T.C. Yuan, S.Y. Xie, M. Zhang, K.C. Zhou, and P. Cao, *Scr. Mater.* 143, 25. (2018).
21. A.M. Okoro, S.S. Lephuthing, S.R. Oke, O.E. Falodun, M.A. Awotunde, and P.A. Olubambi, *JOM* 71, 567. (2019).
22. M.R. Akbarpour, and S.M. Javadhesari, *JOM* 72, 3262. (2020).
23. N. Yang, Z. Wang, L. Chen, Y. Wang, and Y.B. Zhu, *Int. J. Refract. Met. Hard Mater.* 28, 198. (2010).
24. J. Li, B. Wang, H. Ji, J. Zhou, X. Fu, and X. Huang, *Int. J. Adv. Manuf. Tech.* 94, 2149. (2018).
25. M.Y. Zhan, Z.H. Chen, H.G. Yan, and W.J. Xia, *J. Mater. Process. Technol.* 182, 174. (2007).
26. A. Chaijaruwanich, R.J. Dashwood, P.D. Lee, and H. Nagami, *Acta Mater.* 54, 5185. (2006).
27. K. Chen, K. Liu, H. Chen, and Y. Yang, *Comput. Mater. Sci.* 91, 303. (2014).
28. H. Shang, A. Mohanram, E. Olevsky, and R.K. Bordia, *J. Eur. Ceram. Soc.* 36, 2937. (2016).
29. H.S. Kim, *J. Mater. Process. Technol.* 123, 319. (2002).
30. X.W. Du, Z. Zhang, Y. Wang, J.L. Wang, W.M. Wang, H. Wang, and Z.Y. Fu, *J. Am. Ceram. Soc.* 98, 1400. (2015).
31. D.W. Kim, H.T. Son, and J.H. Lee, *J. Alloys Compd.* 528, 146. (2012).
32. A.R. Deshmukh, T. Sundararajan, R.K. Dube, and S. Bhargava, *J. Mater. Process. Technol.* 84, 56. (1998).
33. Y.S. Kwon, G. Son, J. Suh, and K.T. Kim, *J. Am. Ceram. Soc.* 77, 3137. (1994).
34. H.M. Jang, W.E. Rhine, and H.K. Bowen, *J. Am. Ceram. Soc.* 72, 954. (1989).
35. C. Wang, and S.H. Chen, *Sci. China: Phys. Mech. Astron.* 55, 1051. (2012).
36. N.C. Ferreri, R. Pokharel, V. Ivescu, D.W. Brown, M. Knezevic, J.S. Park, M.A. Torrez, and G.T. Gray III., *Acta Mater.* 195, 59. (2020).
37. K. Mumtaz, S. Takahashi, J. Echigoya, Y. Kamada, L. Zhang, H. Kikuchi, K. Ara, and M. Sato, *J. Mater. Sci.* 39, 1997. (2004).
38. M. Yasuoka, P. Wang, K. Zhang, Z. Qiu, K. Kusaka, Y. Pyoun, and R. Murakami, *Surf. Coat. Technol.* 218, 93. (2013).
39. Z. Dai, R. Ding, Z. Yang, C. Zhang, and H. Chen, *Acta Mater.* 152, 288. (2018).
40. R. Wei, M. Enomoto, R. Hadian, H.S. Zurob, and G.R. Purdy, *Acta Mater.* 61, 697. (2013).
41. H. Luo, J. Shi, C. Wang, W. Cao, X. Sun, and H. Dong, *Acta Mater.* 59, 4002. (2011).
42. R. Ding, Z. Dai, M. Huang, Z. Yang, C. Zhang, and H. Chen, *Acta Mater.* 147, 59. (2018).
43. C. Lopez, A. Kvrryan, S. Kasnakjian, A. Coronado, S. Sujit-tosakul, O. Villalpando, and V.A. Ravi, *JOM* 67, 61. (2015).
44. Y. Zou, Y.B. Xu, Z.P. Hu, X.L. Gu, F. Peng, X.D. Tan, S.Q. Chen, D.T. Han, R.D.K. Misra, and G.D. Wang, *Mater. Sci. Eng. A* 675, 153. (2016).
45. S.F. Peterson, M.C. Mataya, and D.K. Matlock, *JOM* 49, 54. (1997).
46. J. Trzaska, *Arch. Metall. Mater.* 60, 181. (2015).
47. Q. Shan, Z. Li, Y. Jiang, R. Zhou, and Y. Sui, *J. Mater. Sci. Technol.* 29, 720. (2013).
48. K.W. Andrews, *J. Iron Steel Res. Int.* 203, 721. (1965).
49. X. Rong, S. Liu, Y. Li, B. Hu, M. Enomoto, H. Guo, and C. Shang, *Mater. Sci. Eng. A* 760, 47. (2019).
50. S.D. de Souza, P.S. Moreira, and G.L. de Faria, *Mater. Res. - Ibero-am. J. Mater.* 23 (2020).
51. T.S. Wang, M. Zhang, Y.H. Wang, J. Yang, and F.C. Zhang, *Scr. Mater.* 68, 162. (2013).
52. M. Zhang, T.S. Wang, Y.H. Wang, J. Yang, and F.C. Zhang, *Mater. Sci. Eng. A* 568, 123. (2013).
53. J. Erneman, L. Nylöf, J. Nilsson, and H. Andrén, *Mater. Sci. Technol.* 20, 1245. (2004).
54. A.W. Wilson, J.D. Madison, and G. Spanos, *Scr. Mater.* 45, 1335. (2001).
55. I.G. Shaaban, Y.B. Shaheen, E.L. Elsayed, O.A. Kamal, and P.A. Adesina, *Constr. Build. Mater.* 171, 802. (2018).
56. A.B. Kale, A. Bag, J.H. Hwang, E.G. Castle, M.J. Reece, and S.H. Choi, *Mater. Sci. Eng. A* 707, 362. (2017).
57. F. Wakai, K. Katsura, S. Kanchika, Y. Shinoda, T. Akatsu, and K. Shinagawa, *Acta Mater.* 109, 292. (2016).
58. M. Zhang, H. Chen, Y. Wang, S. Wang, R. Li, S. Li, and Y.D. Wang, *J. Mater. Sci. Technol.* 35, 1779. (2019).

59. E. Ishimaru, H. Hamasaki, and F. Yoshida, *J. Mater. Process. Technol.* 223, 34. (2015).
60. A. Kundu, and D.P. Field, *Mater. Sci. Eng. A* 667, 435. (2016).
61. B. Babu, and L.E. Lindgren, *Int. J. Plast.* 50, 94. (2013).
62. M.B. Karimi, H. Arabi, A. Khosravani, and J. Samei, *J. Mater. Process. Technol.* 203, 349. (2008).
63. P. Dastur, A. Zarei-Hanzaki, R. Rahimi, M. Moallemi, V. Klemm, B.C. De Cooman, and J. Mola, *Metall. Mater. Trans. A* 50, 4550. (2019).
64. D.G. Rodrigues, G. Maria, N. Viana, and D.B. Santos, *Mater. Charact.* 150, 138. (2019).
65. H. Matsumoto, S. Watanabe, and S. Hanada, *Mater. Sci. Eng. A* 448, 39. (2007).
66. S.M. Na, and A.B. Flatau, *Scr. Mater.* 66, 307. (2012).
67. H.K. Cho, and R.E. Rowlands, *Compos. Sci. Technol.* 67, 2877. (2007).
68. H. Li, M.W. Fu, J. Lu, and H. Yang, *Int. J. Plast.* 27, 147. (2011).
69. Y. Liu, L. Kang, and H.B. Ge, *J. Constr. Steel. Res.* 158, 381. (2019).
70. M. Behzadinasab, and J.T. Foster, *Int. J. Fract.* 224, 261. (2020).
71. S. Zhang, Y. Lu, Z. Shen, C. Zhou, and Y. Lou, *Int. J. Damage Mech.* 29, 1199. (2019).
72. A. Shiga, T. Yamashita, Y. Neishi, and O. Umezawa, *Mater. Trans.* 62, 505. (2021).
73. S.K. Paul, S. Sivaprasad, S. Dhar, and S. Tarafder, *Theor. Appl. Fract. Mec.* 54, 63. (2010).
74. A. Pequegnat, C.J. Hang, M. Mayer, Y. Zhou, J.T. Moon, and J. Persic, *J. Mater. Sci.: Mater. Electron.* 20, 1144. (2009).
75. A. Misra, X. Zhang, D. Hammon, and R.G. Hoagland, *Acta Mater.* 53, 221. (2005).
76. T. Hama, R. Namakawa, Y. Maeda, and Y. Maeda, *Mater. Trans.* 62, 1124. (2021).
77. X. Li, L.L. Wei, L.Q. Chen, Y. Zhao, and R. Misra, *Mater. Charact.* 144, 575. (2018).
78. D.J. Dunstan, and A.J. Bushby, *Int. J. Plast.* 53, 56. (2014).
79. N. Hansen, *Scr. Mater.* 51, 801. (2004).
80. J.E. Jin, Y.S. Jung, and Y.K. Lee, *Mater. Sci. Eng. A* 449–451, 786. (2007).
81. D.A. Hughes, and N. Hansen, *Acta Mater.* 148, 374. (2018).
82. H.L. Chang, C.T. Kuo, and M.S. Liang, *Microelectron. Eng.* 88, 1623. (2011).
83. K.O. Pedersen, I. Westermann, T. Furu, T.B. Rvik, and O.S. Hopperstad, *Mater. Des.* 70, 31. (2015).
84. Y.C. Bai, Y.Q. Yang, Z.F. Xiao, M.K. Zhang, and D. Wang, *Mater. Des.* 140, 257. (2018).
85. X. Chen, G.S. Huang, S.S. Liu, T.Z. Han, B. Jiang, A.T. Tang, Y.T. Zhu, and F.S. Pan, *Trans. Nonferrous Met. Soc. China* 29, 437. (2019).
86. Y.P. Zheng, W.D. Zeng, D. Li, H.Y. Ma, P.H. Zhang, and X. Ma, *J. Alloys Compd.* 799, 267. (2019).

**Publisher's Note** Springer Nature remains neutral with regard to jurisdictional claims in published maps and institutional affiliations.